The Astronomical Journal, 143:29 (12pp), 2012 February doi:10.1088/0004-6256/143/2/29
© 2012. The American Astronomical Society. All rights reserved. Printed in the U.S.A.

AGE AND STRUCTURE PARAMETERS OF THE REMOTE M31 GLOBULAR CLUSTER B514 BASED ON *HST*, 2MASS, *GALEX*, AND BATC OBSERVATIONS

Jun Ma[1,2], Song Wang[1,3], Zhenyu Wu[1], Zhou Fan[1], Tianmen Zhang[1], Jianghua Wu[1], Xu Zhou[1], Zhaoji Jiang[1], and Jiansheng Chen[1]
[1] National Astronomical Observatories, Chinese Academy of Sciences, Beijing 100012, China; majun@nao.cas.cn
[2] Key Laboratory of Optical Astronomy, National Astronomical Observatories, Chinese Academy of Sciences, Beijing 100012, China
[3] Graduate University of Chinese Academy of Sciences, A19 Yuquan Road, Shijingshan District, Beijing 100049, China
Received 2011 March 17; accepted 2011 November 2; published 2011 December 15

ABSTRACT

B514 is a remote M31 globular cluster (GC) which is located at a projected distance of $R_p \simeq 55$ kpc. Deep observations with the Advanced Camera for Surveys on the *Hubble Space Telescope* are used to provide accurate integrated light and star counts of B514. By coupling the analysis of the distribution of the integrated light with star counts, we are able to reliably follow the profile of the cluster out to $\sim 40''$. Based on the combined profile, we study in detail its surface brightness distribution in the F606W and F814W filters and determine its structural parameters by fitting a single-mass isotropic King model. The results showed that the surface brightness distribution departs from the best-fit King model for $r > 10''$. B514 is quite flat in the inner region and has a larger half-light radius than the majority of normal GCs of the same luminosity. It is interesting that, in the M_V versus log R_h plane, B514 lies nearly on the threshold for ordinary GCs as defined by Mackey & van den Bergh. In addition, B514 was observed as part of the Beijing–Arizona–Taiwan–Connecticut (BATC) Multicolor Sky Survey, using 13 intermediate-band filters covering a wavelength range of 3000–8500 Å. Based on aperture photometry, we obtain its spectral energy distributions (SEDs) as defined by the 13 BATC filters. We determine the cluster's age and mass by comparing its SEDs (from 2267 to 20000 Å, comprised of photometric data from the near-ultraviolet band of the *Galaxy Evolution Explorer*, 5 Sloan Digital Sky Survey bands, 13 BATC intermediate-band filters, and Two Micron All Sky Survey near-infrared JHK_s filters) with theoretical stellar population synthesis models, resulting in an age of 11.5 ± 3.5 Gyr. This age confirms the previous suggestion that B514 is an old GC in M31. B514 has a mass of $0.96–1.08 \times 10^6\ M_\odot$ and is a medium-mass GC in M31.

Key words: galaxies: evolution – galaxies: individual (M31) – galaxies: star clusters: individual (B514)

1. INTRODUCTION

In hierarchical cosmological models, galaxies are built up through the continuous accretion and merging of smaller galaxies. The signature of these system assembly processes is expected to be seen in the outskirts of a galactic halo. Globular clusters (GCs), as luminous compact objects that are found out to distant radii in the halos of massive galaxies, can serve as excellent tracers of substructures in the outer region of their parent galaxy. Thus, detailed studies on GCs in the outer halos of the local galaxies are very important.

M31, with a distance modulus of 24.47 (Holland 1998; Stanek & Garnavich 1998; McConnachie et al. 2005), is an ideal nearby galaxy for studying GCs since it is very near and contains more GCs than all other Local Group galaxies combined (Battistini et al. 1987; Racine 1991; Harris 1991; Fusi Pecci et al. 1993). The study of GCs in M31 was initiated by Hubble (1932), who discovered 140 GC candidates with $m_{\rm pg} \leqslant 18$ mag. Following Hubble's discovery, a number of catalogs of GC candidates were published. For example, the Bologna Group (Battistini et al. 1980, 1987, 1993) did independent searches of GC candidates and compiled them with their own Bologna number. The Bologna catalog contains a total of 827 objects, and all the objects were classified into five classes by the authors' degree of confidence. Of these candidates, 353 were considered to be class A or class B with a high level of confidence, and the others fell into classes C, D, or E. V magnitude and $B-V$ color for most candidates were given in the Bologna catalog. There are recent works dealing with the searches and the catalogs of M31 GCs (e.g., Mochejska et al. 1998; Barmby & Huchra 2001; Galleti et al. 2004, 2006, 2007; Huxor et al. 2005, 2008, 2011; Kim et al. 2007; Mackey et al. 2006, 2007, 2010; Martin et al. 2006; Caldwell et al. 2009, 2011; Peacock et al. 2010). The continued importance of the study of GCs in this galaxy has been reviewed by Barmby et al. (2000).

From the spatial structure and internal stellar kinematics of GCs, we can obtain information on both their formation conditions and dynamical evolution within the tidal fields of their host galaxies. For example, the structural parameters of GCs indicate the timescales on which the cluster is bound to dissolve. However, the integrated properties of GCs, such as age and metallicity, are believed to reflect conditions in the early stages of galaxy formation (Brodie & Strader 2006).

The most direct method to determine a cluster's age is to employ main-sequence photometry, since the absolute magnitude of the main-sequence turnoff is predominantly affected by age (see Puzia et al. 2002 and references therein). However, until recently (cf. Perina et al. 2009), this method was only applied to the star clusters in the Milky Way and its satellites (e.g., Rich et al. 2001), although Brown et al. (2004) estimated the age of an M31 GC using extremely deep images observed with the *Hubble Space Telescope* (*HST*) Advanced Camera for Surveys (ACS). Generally, the ages of extragalactic star clusters are determined by comparing their observed spectral energy distributions (SEDs) and/or spectroscopy with the predictions of Simple Stellar Population (SSP) models (Williams & Hodge 2001a, 2001b; de Grijs et al. 2003a, 2003b, 2003c; Bik et al. 2003; Jiang et al. 2003; Beasley et al. 2004; Puzia et al. 2005; Fan et al. 2006; Ma et al. 2006a, 2007b, 2009a, 2009b, 2011; Caldwell et al. 2009, 2011; Wang et al. 2010; Perina et al. 2011).

M31 GC B514 (B for "Bologna;" see Battistini et al. 1987), which was detected by Galleti et al. (2005) based on the Extended Source Catalog (XSC) sources of the All Sky Data Release of the Two Micron All Sky Survey (2MASS) within a $\sim 9^\circ \times 9^\circ$ area centered on M31, is the outermost cluster known in M31 at that time, located at a projected distance of $R_p \simeq 55$ kpc. Now, many new members of the M31 halo GC system, which are extending to very large radii, have been discovered (e.g., Huxor et al. 2005, 2008, 2011; Mackey et al. 2006, 2007, 2010; Martin et al. 2006).

Galleti et al. (2006) presented a deep color–magnitude diagram (CMD) for B514 in F606W and F814W photometry obtained with the ACS/*HST*, which reveals a steep red giant branch and a horizontal branch extending blueward of the instability strip showing that B514 is a classical old metal-poor GC. Federici et al. (2007) studied the density profile of B514 based on the same *HST*/ACS observations as Galleti et al. (2006), and they found that the light and the star-count profiles show a departure from the best-fit empirical models of King (1962) for $r \geqslant 8''$—as a surface brightness excess at large radii—and that the star-count profile shows a clear break in the correspondence of the estimated tidal radius. They also found that B514 has a significantly larger half-light radius than ordinary GCs of the same luminosity. Clementini et al. (2009) identified a rich harvest of RR Lyrae stars in B514, based on *HST* Wide Field Planetary Camera 2 (WFPC2) and *HST*/ACS time-series observations.

Since B514 is located in the halo of M31, i.e., far away from the galaxy's disk, it is (for all practical purposes) only affected by the Galactic foreground extinction. The foreground Galactic reddening in the direction of M31 has been discussed by many authors (e.g., van den Bergh 1969; McClure & Racine 1969; Frogel et al. 1980; Fusi Pecci et al. 2005), and nearly similar values were determined, such as $E(B-V) = 0.08$ by van den Bergh (1969), 0.11 by McClure & Racine (1969) and Hodge (1992), and 0.08 by Frogel et al. (1980). We argue that the reddening value of B514 should not be smaller than the foreground Galactic reddening in the direction of M31. In this paper, we adopt the reddening value of $E(B-V) = 0.10$ from Galleti et al. (2006). The reddening law from Cardelli et al. (1989) is employed in this paper. In addition, throughout this paper we adopt a distance to M31 of 783 ± 25 kpc ($1''$ subtends 3.8 pc), corresponding to a distance modulus of $(m-M)_0 = 24.47 \pm 0.07$ mag (McConnachie et al. 2005).

In this paper, we describe the details of the observations and our approach to the data reduction with the *HST*/ACS and the Beijing–Arizona–Taiwan–Connecticut (BATC) system in Sections 2 and 3. We will study in detail the surface distribution of B514 using the King (1966) models, which were developed by Michie (1963) and King (1966) based on the assumption that GCs are formed by single-mass, isotropic, lowered isothermal spheres (hereafter "King models"). We determine the age and mass of B514 by comparing observational SEDs with population synthesis models in Section 4. We provide a summary in Section 5.

2. OBSERVATION AND PHOTOMETRIC DATA WITH *HST*/ACS

The images of B514 used in this paper were observed with the ACS/Wide Field Camera (WFC) in the F606W and F814W filters on 2005 July 19 (program ID GO 10394; PI: N. Tanvir), covering the period 2005 July 19–20 in F606W (total $t_{\rm exp} = 1776$ s) and F814W (total $t_{\rm exp} = 2505$ s). Upon retrieval from the STScI archive, all images were processed using the standard ACS calibration pipeline, in which bias and dark subtractions, flat-field division, and the masking of known bad pixels are included. Subsequently, photometric header keywords are populated. In the final stage of the pipeline, the MultiDrizzle software is used to correct the geometric distortion present in the images. Finally, any cosmic rays are rejected while individual images in each band are combined into a final single image. We checked the images and did not find saturated cluster stars. Figure 1 shows the images observed with the ACS/WFC in F606W and F814W. The ACS/WFC spatial resolution is $0\farcs05$ pixel^{-1}.

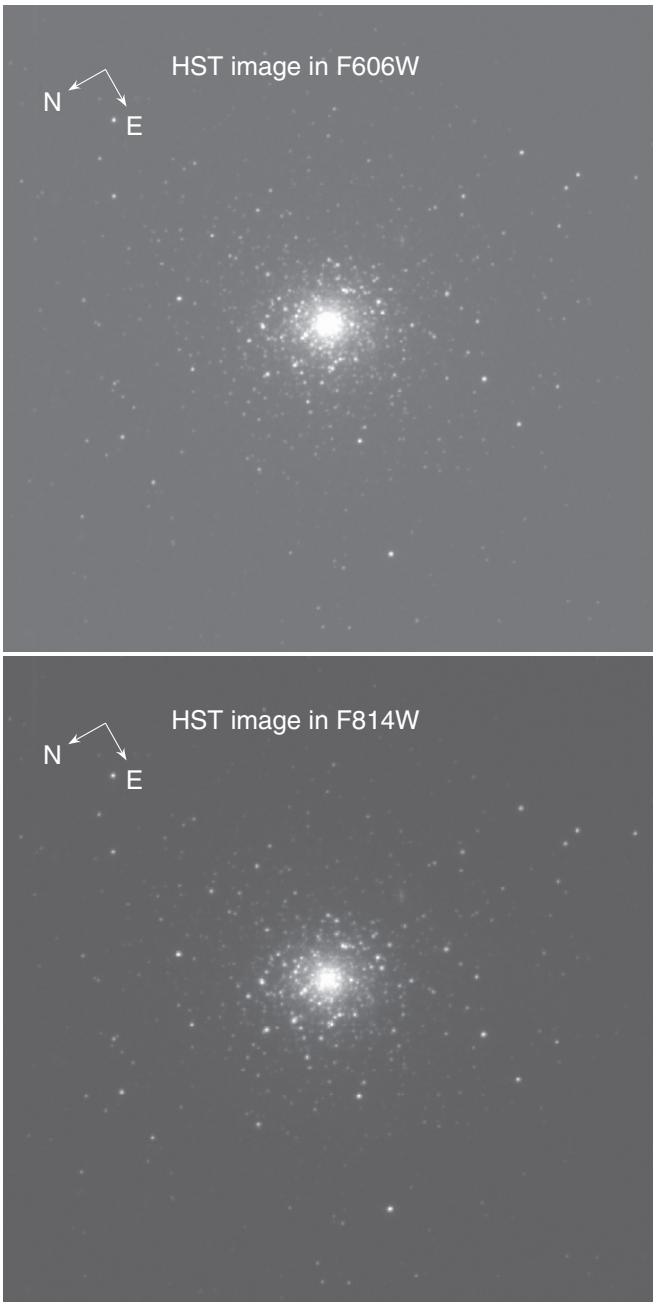

Figure 1. Images of GC B514 observed in the F606W and F814W filters of ACS/*HST*. The image size is $20'' \times 20''$ for each panel.

2.1. Ellipticity, Position Angle, and Surface Brightness Profile

Surface photometry of the cluster is obtained from the drizzled images using the IRAF task ELLIPSE. Its center position

Table 1
B514: Ellipticity, ϵ, and Position Angle (P.A.) as a Function of the Semimajor Axis, a, in the F606W Filter of *HST* ACS/WFC

a (arcsec)	ϵ	P.A. (deg)	a (arcsec)	ϵ	P.A. (deg)
0.0260	0.360 ± 0.082	159.5 ± 8.3	0.1752	0.598 ± 0.046	147.9 ± 3.4
0.0287	0.380 ± 0.087	158.6 ± 8.3	0.1928	0.150 ± 0.150	150.4 ± 32.0
0.0315	0.402 ± 0.092	157.7 ± 8.5	0.2120	0.150 ± 0.183	107.3 ± 38.4
0.0347	0.426 ± 0.098	156.9 ± 8.6	0.2333	0.171 ± 0.111	84.8 ± 20.6
0.0381	0.449 ± 0.104	155.6 ± 8.8	0.2566	0.203 ± 0.066	76.4 ± 10.5
0.0420	0.474 ± 0.112	154.3 ± 9.2	0.2822	0.199 ± 0.049	79.3 ± 8.0
0.0461	0.503 ± 0.123	153.1 ± 9.7	0.3105	0.205 ± 0.062	94.7 ± 9.8
0.0508	0.535 ± 0.134	152.3 ± 10.2	0.3415	0.210 ± 0.059	102.4 ± 9.1
0.0558	0.570 ± 0.133	151.6 ± 9.7	0.3757	0.197 ± 0.059	112.5 ± 9.5
0.0614	0.596 ± 0.137	150.6 ± 9.7	0.4132	0.171 ± 0.066	129.9 ± 12.1
0.0676	0.622 ± 0.146	149.6 ± 10.1	0.4545	0.090 ± 0.094	143.8 ± 31.9
0.0743	0.649 ± 0.159	148.8 ± 10.8	0.5000	0.090 ± 0.071	20.8 ± 23.6
0.0818	0.678 ± 0.134	147.8 ± 8.8	0.5500	0.123 ± 0.041	95.8 ± 10.1
0.0899	0.694 ± 0.114	147.4 ± 7.4	0.6050	0.102 ± 0.024	117.4 ± 7.2
0.0989	0.686 ± 0.092	146.9 ± 6.0	0.6655	0.119 ± 0.024	98.6 ± 6.2
0.1088	0.650 ± 0.075	145.4 ± 5.0	0.7321	0.158 ± 0.032	93.4 ± 6.2
0.1197	0.636 ± 0.059	146.1 ± 4.0	0.8053	0.067 ± 0.049	54.6 ± 21.3
0.1317	0.619 ± 0.050	146.6 ± 3.6	0.8858	0.065 ± 0.034	4.8 ± 15.5
0.1448	0.636 ± 0.037	146.6 ± 2.7	0.9744	0.067 ± 0.096	132.5 ± 42.6
0.1593	0.610 ± 0.064	147.1 ± 4.5			

was fixed at a value derived by an object locator of the ELLIPSE task; however, an initial center position was determined by centroiding. Elliptical isophotes were fitted to the data with no sigma clipping. We ran two passes of the ELLIPSE task, with the first pass ran in the usual way, with ellipticity and position angle (P.A.) allowed to vary with the isophote semimajor axis. In the second pass, surface brightness profiles on fixed, zero-ellipticity isophotes were measured, since we chose to fit circular models for the intrinsic cluster structure and the point-spread function (PSF) as Barmby et al. (2007) did (see Section 2.3 for details). The background value was derived as the mean of a region of 100×100 pixels in "empty" areas far away from the cluster. We performed the photometric calibration using the results of Sirianni et al. (2005): 26.398 in F606W zero points and 25.501 in F814W zero points. Magnitudes are derived in the ACS/WFC VEGAMAG system.

Tables 1 and 2 list the ellipticity, $\epsilon = 1 - b/a$, and the P.A. as a function of the semimajor axis length, a, from the center of annulus in the F606W and F814W filters, respectively. These observables have also been plotted in Figure 2; the errors were generated by the IRAF task ELLIPSE, in which the ellipticity errors are obtained from the internal errors in the harmonic fit, after removal of the first and second fitted harmonics. From Table 1 and Figure 2, we can see that the values of ellipticity and P.A. cannot be obtained beyond 0.″9744 in the F606W filter because of low signal-to-noise ratio (S/N). In addition, Figure 2 shows that the ellipticity varies significantly with position along the semimajor axis radius smaller than ∼0.″1752. Beyond ∼0.″1752, the ellipticity does not vary significantly as a function of the cluster's semimajor axis. The P.A. does not vary as a function of the cluster's semimajor axis within ∼0.″1752 because of high S/N; however, beyond this position, it varies significantly with great errors because of low S/N.

Tables 3 and 4 list the surface brightness profile, μ, of B514 and its integrated magnitude, m, as a function of radius in the F606W and F814W filters, respectively. The errors in the surface brightness were generated by the IRAF task ELLIPSE in which they are obtained directly from the root mean square scatter

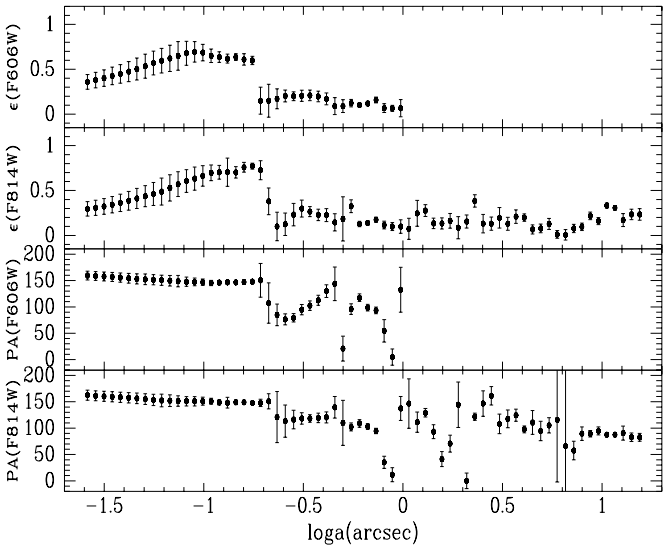

Figure 2. Ellipticity and P.A. as a function of the semimajor axis in the F606W and F814W filters of ACS/*HST*.

of the intensity data along the zero-ellipticity isophotes. In addition, the surface photometries at radii where the ellipticity and P.A. cannot be measured are obtained based on the last ellipticity and P.A. as the IRAF task ELLIPSE is designed.

In order to derive the surface brightness profile of B514 in its outer region, we use the profile from star counts. We used the DOLPHOT[4] photometry software (Dolphin 2000a), specifically the ACS module, to photometer our images. DOLPHOT performs PSF fitting using PSFs especially tailored to the ACS camera. Photometry was done simultaneously on all the flat-fielded images from the STScI archive (both filters) relative to a deep reference image—we used the drizzled combination of the F606W image. DOLPHOT accounts for the hot-pixel and cosmic-ray masking information attached to each flat-fielded image, fits the sky locally around each detected source, and

[4] http://americano.dolphinsim.com/dolphot/

Table 2
B514: Ellipticity, ϵ, and Position Angle (P.A.) as a Function of the Semimajor Axis, a, in the F814W Filter of *HST* ACS/WFC

a (arcsec)	ϵ	P.A. (deg)	a (arcsec)	ϵ	P.A. (deg)
0.0260	0.296 ± 0.081	162.5 ± 9.5	0.6655	0.139 ± 0.026	103.1 ± 5.6
0.0287	0.308 ± 0.084	161.4 ± 9.5	0.7321	0.175 ± 0.028	94.5 ± 5.1
0.0315	0.323 ± 0.087	160.4 ± 9.5	0.8053	0.116 ± 0.043	35.2 ± 11.4
0.0347	0.342 ± 0.091	159.5 ± 9.6	0.8858	0.099 ± 0.044	11.7 ± 13.4
0.0381	0.363 ± 0.097	158.5 ± 9.7	0.9744	0.099 ± 0.075	137.4 ± 22.8
0.0420	0.386 ± 0.104	157.6 ± 9.9	1.0718	0.074 ± 0.117	146.5 ± 46.9
0.0461	0.412 ± 0.112	156.6 ± 10.1	1.1790	0.246 ± 0.144	111.3 ± 19.3
0.0508	0.437 ± 0.117	155.1 ± 10.2	1.2969	0.277 ± 0.066	129.1 ± 8.1
0.0558	0.462 ± 0.128	153.6 ± 10.7	1.4266	0.134 ± 0.058	93.4 ± 13.2
0.0614	0.488 ± 0.150	152.5 ± 12.0	1.5692	0.134 ± 0.062	41.3 ± 14.2
0.0676	0.529 ± 0.146	152.0 ± 11.1	1.7261	0.162 ± 0.082	70.6 ± 16.1
0.0743	0.571 ± 0.138	151.5 ± 10.0	1.8987	0.086 ± 0.124	144.4 ± 43.2
0.0818	0.606 ± 0.127	151.0 ± 8.9	2.0886	0.155 ± 0.073	0.1 ± 14.8
0.0899	0.633 ± 0.129	150.9 ± 8.8	2.2975	0.384 ± 0.069	121.7 ± 6.8
0.0989	0.663 ± 0.114	151.1 ± 7.6	2.5272	0.131 ± 0.103	146.7 ± 24.2
0.1088	0.697 ± 0.087	151.0 ± 5.6	2.7800	0.131 ± 0.074	161.3 ± 17.5
0.1197	0.703 ± 0.077	148.9 ± 5.0	3.0580	0.196 ± 0.114	108.0 ± 18.6
0.1317	0.704 ± 0.157	148.3 ± 10.1	3.3638	0.130 ± 0.072	117.6 ± 16.9
0.1448	0.702 ± 0.064	149.1 ± 4.4	3.7001	0.209 ± 0.075	124.5 ± 11.4
0.1593	0.759 ± 0.055	149.1 ± 3.6	4.0701	0.199 ± 0.041	97.7 ± 6.5
0.1752	0.772 ± 0.033	147.9 ± 2.2	4.4772	0.067 ± 0.051	110.7 ± 22.6
0.1928	0.726 ± 0.106	147.9 ± 6.9	4.9249	0.078 ± 0.048	94.6 ± 18.3
0.2120	0.380 ± 0.149	150.9 ± 14.4	5.4174	0.128 ± 0.061	105.3 ± 14.5
0.2333	0.100 ± 0.159	121.0 ± 48.4	5.9591	0.011 ± 0.043	115.7 ± 118.0
0.2566	0.125 ± 0.125	113.3 ± 30.5	6.5550	0.007 ± 0.059	65.8 ± 244.4
0.2822	0.232 ± 0.125	116.3 ± 17.7	7.2105	0.078 ± 0.046	57.5 ± 17.6
0.3105	0.299 ± 0.094	118.4 ± 10.9	7.9316	0.096 ± 0.041	89.4 ± 12.8
0.3415	0.265 ± 0.056	118.4 ± 7.2	8.7247	0.218 ± 0.042	89.4 ± 6.1
0.3757	0.229 ± 0.064	119.4 ± 9.1	9.5972	0.160 ± 0.039	94.7 ± 7.6
0.4132	0.226 ± 0.072	120.4 ± 10.5	10.5569	0.333 ± 0.029	87.5 ± 3.0
0.4545	0.146 ± 0.096	139.6 ± 20.5	11.6126	0.307 ± 0.023	87.5 ± 2.6
0.5000	0.184 ± 0.246	110.0 ± 42.6	12.7738	0.171 ± 0.072	90.6 ± 13.3
0.5500	0.325 ± 0.071	102.3 ± 7.5	14.0512	0.234 ± 0.058	82.6 ± 8.1
0.6050	0.127 ± 0.030	108.9 ± 7.3	15.4564	0.234 ± 0.064	82.6 ± 7.4

automatically applies the correction for the charge-transfer efficiency (CTE; Dolphin 2000b). It then transforms the instrumental magnitude to the VEGAMAG system (Dolphin 2000b). A variety of quality information is listed with each detected object, including the object type (stellar, extended, etc.), χ^2 of the PSF fit, the sharpness and roundness of the object, and a "crowding" parameter which describes how much brighter an object would have been had neighboring objects not been fitted simultaneously. We used the quality information provided by DOLPHOT to clean the resulting detection lists, selecting only stellar detections, with valid photometry on all input images, a global sharpness parameter between −0.3 and 0.3 in each filter, and a crowding parameter of less than 0.25 in each filter.

We joined the two profiles into one based on the method of Federici et al. (2007). This involves matching the intensity scales of the two profiles by fitting both profiles to smooth curves in the region $r = 9''$–$16''$. The star-count profile is listed in Table 5. The errors for the star counts take into account Poisson statistical uncertainties. The joined profile covered the full $0'' < r \leqslant 40''$ range as shown in Figure 3.

2.2. Point-spread Function

At a distance of 783 kpc, the ACS/WFC has a scale of $0\farcs05 = 0.19\,\mathrm{pc\,pixel^{-1}}$, and thus M31 clusters are clearly resolved with it. Their observed core structures, however, are still affected by the PSF. We chose not to deconvolve the data, instead fitting structural models after convolving them with a simple analytic description of the PSF as Barmby et al. (2007) and McLaughlin et al. (2008) did (see Barmby et al. 2007; McLaughlin et al. 2008; Ma 2011 for details). In addition, since this PSF formula is radially symmetric and the models of King (1966) we fit are intrinsically spherical, the convolved models to be fitted to the data are also circularly symmetric.

2.3. Models and Fits

2.3.1. Structural Models

After elliptical galaxies, GCs are the best understood and most thoroughly modeled class of stellar systems. For example, a large majority of the ∼150 Galactic GCs have been fitted by the simple models of single-mass, isotropic, lowered isothermal spheres developed by Michie (1963) and King (1966; i.e., King models), yielding comprehensive catalogs of cluster structural parameters and physical properties (see McLaughlin & van der Marel 2005 and references therein). For extragalactic GCs, *HST* imaging data have been used to fit the King models to a large number of GCs in M31 (e.g., Barmby et al. 2002, 2007, 2009, and references therein), M33 (Larsen et al. 2002), and NGC 5128 (e.g., Harris et al. 2002; McLaughlin et al. 2008, and references therein). In addition, there are other models used to fit the surface profile of GCs, including those by Wilson (1975), Elson et al.

Table 3
B514: Surface Brightness, μ, and Integrated Magnitude, m, as a Function of the Radius in the F606W Filter of *HST* ACS/WFC

R (arcsec)	μ (mag arcsec^{-2})	m (mag)	R (arcsec)	μ (mag arcsec^{-2})	m (mag)
0.0260	16.438 ± 0.034	22.868	0.6655	18.091 ± 0.055	17.008
0.0287	16.445 ± 0.038	22.868	0.7321	18.212 ± 0.071	16.900
0.0315	16.452 ± 0.043	22.868	0.8053	18.374 ± 0.080	16.804
0.0347	16.461 ± 0.048	22.868	0.8858	18.588 ± 0.079	16.705
0.0381	16.470 ± 0.054	22.868	0.9744	18.799 ± 0.086	16.615
0.0420	16.480 ± 0.062	22.868	1.0718	18.808 ± 0.134	16.531
0.0461	16.491 ± 0.070	22.868	1.1790	18.953 ± 0.289	16.434
0.0508	16.503 ± 0.080	21.221	1.2969	19.283 ± 0.175	16.362
0.0558	16.517 ± 0.090	21.221	1.4266	19.545 ± 0.170	16.283
0.0614	16.534 ± 0.102	21.221	1.5692	19.839 ± 0.141	16.212
0.0676	16.553 ± 0.114	21.221	1.7261	19.890 ± 0.243	16.149
0.0743	16.574 ± 0.126	20.628	1.8987	20.258 ± 0.141	16.087
0.0818	16.598 ± 0.135	20.628	2.0886	20.308 ± 0.232	16.024
0.0899	16.623 ± 0.146	20.628	2.2975	20.770 ± 0.147	15.968
0.0989	16.650 ± 0.159	20.628	2.5272	20.905 ± 0.220	15.917
0.1088	16.680 ± 0.156	20.281	2.7800	21.196 ± 0.162	15.866
0.1197	16.708 ± 0.148	19.809	3.0580	21.565 ± 0.252	15.819
0.1317	16.713 ± 0.143	19.809	3.3638	21.967 ± 0.094	15.785
0.1448	16.725 ± 0.132	19.638	3.7001	22.090 ± 0.274	15.751
0.1593	16.764 ± 0.117	19.254	4.0701	22.568 ± 0.117	15.720
0.1752	16.788 ± 0.102	19.254	4.4772	22.904 ± 0.102	15.695
0.1928	16.810 ± 0.090	19.060	4.9249	23.113 ± 0.115	15.673
0.2120	16.858 ± 0.075	18.837	5.4174	23.359 ± 0.147	15.649
0.2333	16.900 ± 0.054	18.652	5.9591	23.743 ± 0.096	15.622
0.2566	16.959 ± 0.049	18.418	6.5550	24.078 ± 0.101	15.604
0.2822	17.028 ± 0.057	18.341	7.2105	24.331 ± 0.099	15.580
0.3105	17.109 ± 0.074	18.150	7.9316	24.692 ± 0.082	15.560
0.3415	17.199 ± 0.076	17.991	8.7247	25.101 ± 0.116	15.545
0.3757	17.285 ± 0.066	17.835	9.5972	25.328 ± 0.118	15.534
0.4132	17.366 ± 0.060	17.662	10.5569	25.526 ± 0.127	15.518
0.4545	17.439 ± 0.064	17.532	11.6126	25.840 ± 0.164	15.496
0.5000	17.490 ± 0.074	17.382	12.7738	26.212 ± 0.170	15.483
0.5500	17.630 ± 0.072	17.249	14.0512	26.527 ± 0.176	15.469
0.6050	17.881 ± 0.058	17.108	15.4564	26.951 ± 0.233	15.462

Table 4
B514: Surface Brightness, μ, and Integrated Magnitude, m, as a Function of the Radius in the F814W Filter of *HST* ACS/WFC

R (arcsec)	μ (mag arcsec^{-2})	m (mag)	R (arcsec)	μ (mag arcsec^{-2})	m (mag)
0.0260	15.810 ± 0.050	22.224	0.6655	17.332 ± 0.068	16.278
0.0287	15.819 ± 0.055	22.224	0.7321	17.451 ± 0.077	16.166
0.0315	15.828 ± 0.061	22.224	0.8053	17.601 ± 0.105	16.068
0.0347	15.839 ± 0.068	22.224	0.8858	17.837 ± 0.096	15.966
0.0381	15.850 ± 0.076	22.224	0.9744	18.048 ± 0.098	15.875
0.0420	15.862 ± 0.085	22.224	1.0718	18.007 ± 0.179	15.791
0.0461	15.874 ± 0.095	22.224	1.1790	18.194 ± 0.245	15.686
0.0508	15.888 ± 0.107	20.601	1.2969	18.447 ± 0.336	15.613
0.0558	15.903 ± 0.118	20.601	1.4266	18.755 ± 0.190	15.533
0.0614	15.917 ± 0.126	20.601	1.5692	19.082 ± 0.151	15.460
0.0676	15.931 ± 0.135	20.601	1.7261	19.078 ± 0.335	15.394
0.0743	15.947 ± 0.144	20.013	1.8987	19.444 ± 0.186	15.328
0.0818	15.965 ± 0.152	20.013	2.0886	19.540 ± 0.232	15.261
0.0899	15.982 ± 0.160	20.013	2.2975	19.965 ± 0.199	15.203
0.0989	15.999 ± 0.169	20.013	2.5272	20.101 ± 0.259	15.150
0.1088	16.015 ± 0.169	19.656	2.7800	20.402 ± 0.164	15.096
0.1197	16.034 ± 0.159	19.170	3.0580	20.718 ± 0.310	15.045
0.1317	16.024 ± 0.157	19.170	3.3638	21.153 ± 0.126	15.012
0.1448	16.022 ± 0.151	18.989	3.7001	21.253 ± 0.322	14.975
0.1593	16.055 ± 0.137	18.589	4.0701	21.778 ± 0.116	14.944
0.1752	16.072 ± 0.128	18.589	4.4772	22.117 ± 0.088	14.920
0.1928	16.078 ± 0.118	18.384	4.9249	22.297 ± 0.119	14.898
0.2120	16.120 ± 0.098	18.153	5.4174	22.484 ± 0.174	14.874
0.2333	16.171 ± 0.070	17.959	5.9591	22.916 ± 0.113	14.845
0.2566	16.225 ± 0.059	17.715	6.5550	23.213 ± 0.123	14.826
0.2822	16.287 ± 0.070	17.639	7.2105	23.470 ± 0.125	14.800
0.3105	16.367 ± 0.092	17.441	7.9316	23.880 ± 0.088	14.778
0.3415	16.454 ± 0.098	17.275	8.7247	24.263 ± 0.121	14.763
0.3757	16.558 ± 0.089	17.116	9.5972	24.457 ± 0.132	14.752
0.4132	16.646 ± 0.067	16.944	10.5569	24.607 ± 0.158	14.735
0.4545	16.708 ± 0.070	16.814	11.6126	24.935 ± 0.155	14.710
0.5000	16.740 ± 0.082	16.659	12.7738	25.294 ± 0.197	14.697
0.5500	16.878 ± 0.098	16.524	14.0512	25.649 ± 0.231	14.681
0.6050	17.137 ± 0.079	16.380	15.4564	26.034 ± 0.379	14.674

(1987), and Sérsic (1968). In this paper, we fit King models to the density profile of B514 observed with ACS/WFC.

2.3.2. Fits

Our fitting procedure involves computing in full large numbers of King structural models spanning a wide range of fixed values of the appropriate shape parameter W_0 (see McLaughlin & van der Marel 2005, for details). Then, the models are convolved with the ACS/WFC PSF for the F606W and F814W filters (see Barmby et al. 2007 for details):

$$\widetilde{I}^{*}_{\rm mod}(R|r_0) = \iint_{-\infty}^{\infty} \widetilde{I}_{\rm mod}(R'/r_0) \times \widetilde{I}_{\rm PSF}[(x-x'), (y-y')]\, dx'\, dy', \quad (1)$$

where $\widetilde{I}_{\rm mod} \equiv I_{\rm mod}/I_0$ (see McLaughlin et al. 2008 for details). We changed the luminosity density to surface brightness $\widetilde{\mu}^{*}_{\rm mod} = -2.5\,\log[\widetilde{I}^{*}_{\rm mod}]$ before fitting them to the observed surface brightness profile of B514, $\mu = \mu_0 - 2.5\,\log[I(R/r_0)/I_0]$, finding the radial scale r_0 and central surface brightness μ_0, which minimizes χ^2 for every given value of W_0. The (W_0, r_0, μ_0) combination that yields the global minimum $\chi^2_{\rm min}$ over the grid used defines the best-fit model of that type:

$$\chi^2 = \sum_i \frac{[\mu_{\rm obs}(R_i) - \widetilde{\mu}^{*}_{\rm mod}(R_i|r_0)]^2}{\sigma_i^2}, \quad (2)$$

in which σ_i is the error in the surface brightness. Estimates of the 1σ uncertainties on these basic fit parameters follow from their extreme values over the subgrid of fits with $\chi^2/\nu \leqslant \chi^2_{\rm min}/\nu + 1$, where ν is the number of free parameters. Figure 3 shows our best King fits to B514. In Figure 3, open squares are ELLIPSE data points included in the least-squares model fitting, and the asterisks are points not used to constrain the fit; black circles are star-count points included in the χ^2 model fitting, and red circles are star-count points not used to constrain the fits. These observed data points shown by asterisks are included in the radius $R < 2$ pixels $= 0\farcs1$, and the isophotal intensity is dependent on its neighbors. As Barmby et al. (2007) pointed out, the ELLIPSE output contains brightnesses for 15 radii inside 2 pixels, but they are all measured from the same 13 central pixels and are not statistically independent. Thus, to avoid excessive weighting of the central regions of B514 in the fits, we only used intensities at radii $R_{\rm min}$, $R_{\rm min}$ + (0.5, 1.0, 2.0)pixels, or $R > 2.5$ as Barmby et al. (2007) used. Table 6 summarizes the results obtained in this paper.

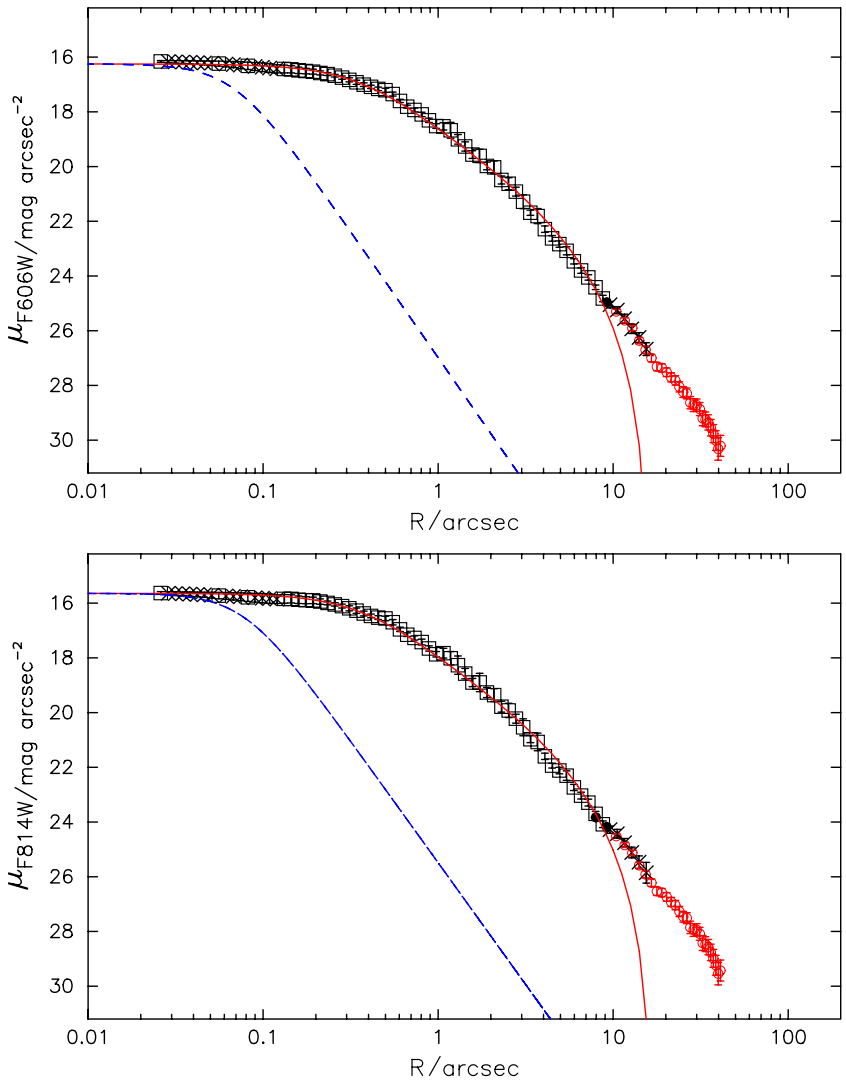

Figure 3. Surface brightness profile of B514 measured in the F606W and F814 filters. The dashed curves (blue) trace the PSF intensity profiles and the solid (red) curves are the PSF-convolved best-fit models. The open squares are ELLIPSE data points and the black circles are star-count profiles included in the χ^2 model fitting, and the asterisks are ELLIPSE data points and the red circles are star-count profiles not used to constrain the fits (see the text for details).

From Figure 3, we can note that the surface brightness distribution departs from the best-fit King model for $r > 10''$, which can be interpreted as the presence of a population of extratidal stars around the cluster. In fact, Federici et al. (2007) have reported this population of extratidal stars (see their Figure 5 and their discussions).

2.4. Distribution of B514 in the M_V versus log R_h Plane

The distribution of stellar systems in the M_V versus log R_h plane can provide interesting information on the evolutionary history of these objects (e.g., van den Bergh & Mackey 2004; Mackey & van den Bergh 2005). In this plane, the half-light radius is an important parameter, which can be used to trace the initial size of a cluster, since it changes little in the evolution process (see Spitzer & Thuan 1972; Henon 1973; Lightman & Shapiro 1978; Murphy et al. 1990 for details).

Recently, van den Bergh & Mackey (2004) and Mackey & van den Bergh (2005) showed that in a plot of luminosity versus half-light radius, the overwhelming majority of normal Galactic GCs lie below (or to the right of) the line

$$\log R_h(\mathrm{pc}) = 0.25 M_V(\mathrm{mag}) + 2.95. \quad (3)$$

Exceptions to this rule are massive clusters, such as M54 and ω Centauri in the Milky Way, and G1 in M31, which are widely believed to be the remnant cores of now defunct dwarf galaxies (Zinnecker et al. 1988; Freeman 1993; Meylan et al. 2001). Because the well-known giant GC NGC 2419 (van den Bergh & Mackey 2004) in the Galaxy and 037-B327 (Ma et al. 2006b) in M31 also lie above this line, it has been speculated that these two objects might also be the remnant cores of dwarf galaxies (however, see de Grijs et al. 2005 for doubts regarding NGC 2419).

With the value of R_h (i.e., r_h) in the F606W filter obtained in this paper, we plot M_V versus log R_h in Figure 4, in which $M_V = -9.02$, which is derived based on $m_V = 15.76$ from Huxor et al. (2008). It is interesting that on this plot B514 is seen to lie nearly on the line defined by Equation (3). Considering the uncertainties of R_h and M_V, a certain conclusion may not be presented here. However, we argued that B514 is a medium-mass GC in M31 (see Section 4.4 for details) and is not as massive as G1 and 037-B327 (see Ma et al. 2006a, 2006b, 2007a, 2009a for details). Furthermore, and for completeness, in Figure 4 we have also included GCs in the Milky Way, M31, and M33. Galactic GCs are from the online database of Harris

Table 5
B514: Surface Brightness Profiles μ from Star Counts

R (arcsec)	μ_{F606W} (mag arcsec^{-2})	R (arcsec)	μ_{F814W} (mag arcsec^{-2})
		7.9625	23.831 ± 0.066
9.1875	24.961 ± 0.072	9.1875	24.181 ± 0.072
10.4125	25.297 ± 0.079	10.4125	24.517 ± 0.079
11.6375	25.622 ± 0.087	11.6375	24.842 ± 0.087
12.8625	25.905 ± 0.095	12.8625	25.125 ± 0.095
14.0875	26.361 ± 0.111	14.0875	25.581 ± 0.111
15.3125	26.694 ± 0.125	15.3125	25.914 ± 0.125
16.5375	26.998 ± 0.138	16.5375	26.218 ± 0.138
17.7625	27.310 ± 0.154	17.7625	26.530 ± 0.154
18.9875	27.360 ± 0.152	18.9875	26.580 ± 0.152
20.2125	27.517 ± 0.158	20.2125	26.737 ± 0.158
21.4375	27.703 ± 0.168	21.4375	26.923 ± 0.168
22.6625	27.816 ± 0.172	22.6625	27.036 ± 0.172
23.8875	28.050 ± 0.186	23.8875	27.270 ± 0.186
25.1125	28.240 ± 0.198	25.1125	27.460 ± 0.198
26.3375	28.292 ± 0.198	26.3375	27.512 ± 0.198
27.5625	28.630 ± 0.226	27.5625	27.850 ± 0.226
28.7875	28.725 ± 0.231	28.7875	27.945 ± 0.231
30.0125	28.722 ± 0.226	30.0125	27.942 ± 0.226
31.2375	28.864 ± 0.237	31.2375	28.084 ± 0.237
32.4625	29.201 ± 0.271	32.4625	28.421 ± 0.271
33.6875	29.242 ± 0.271	33.6875	28.462 ± 0.271
34.9125	29.350 ± 0.280	34.9125	28.570 ± 0.280
36.1375	29.543 ± 0.301	36.1375	28.763 ± 0.301
37.3625	29.761 ± 0.327	37.3625	28.981 ± 0.327
38.5875	30.014 ± 0.362	38.5875	29.234 ± 0.362
39.8125	30.321 ± 0.410	39.8125	29.541 ± 0.410
41.0375	30.208 ± 0.384	41.0375	29.428 ± 0.384

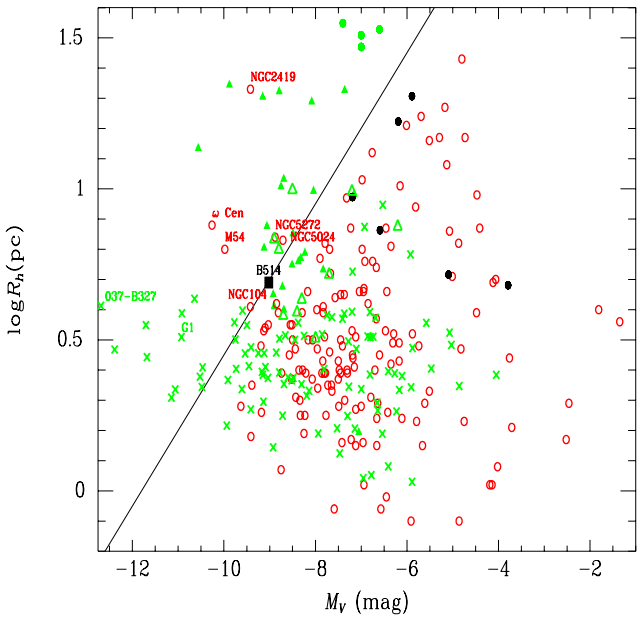

Figure 4. M_V vs. R_h for interesting stellar systems. The plotted line, $\log R_h(\mathrm{pc}) = 0.25 M_V(\mathrm{mag}) + 2.95$, is the threshold for ordinary cluster in this plane as defined by Mackey & van den Bergh (2005). The red circles are Galactic GCs from the online database of Harris (1996; 2010 update), the green crosses are M31 GCs from Barmby et al. (2007), the green filled triangles are M31 young massive clusters from Barmby et al. (2009), the green filled circles are M31 extended clusters from Mackey et al. (2006), the green open triangles are outer M31 GCs from Mackey et al. (2007) the black filled circles are M33 outer halo clusters from Cockcroft et al. (2011), and the black square is B514 derived here.

(1996; 2010 update). This new revision of the McMaster catalog of Galactic GCs is the first update since 2003 and the biggest single revision since the original version of the catalog was published in 1996. The starting points for the present list of structural parameters are the major compilations of McLaughlin & van der Marel (2005) and Trager et al. (1995). McLaughlin & van der Marel (2005) used the same raw data as Trager et al. (1995) and derived structural parameter values from King (1966) dynamical profile models. M31 GCs are from recent compilations of data by Barmby et al. (2007, 2009) and Mackey et al. (2006, 2007). M33 GCs are from Cockcroft et al. (2011). Barmby et al. (2007) derived structural parameters for 34 GCs in M31 based on ACS/*HST* observations, and the derived structural parameters are combined with corrected versions of those measured in an earlier survey in order to construct a comprehensive catalog of structural and dynamical parameters for 93 M31 GCs. Barmby et al. (2009) measured structural parameters for 23 bright young clusters in M31 based on the *HST*/WFPC2 observations and suggested that on average they are larger and more concentrated than typical old clusters. Mackey et al. (2006) determined structural parameters for four extended, luminous GCs in the outskirts of M31 based on ACS/*HST* observations. These objects were discovered by Huxor et al. (2005) and Martin et al. (2006). Mackey et al. (2007) derived structural parameters for 10 classical GCs in the far outer regions of M31 based on ACS/WFC observations. Cockcroft et al. (2011) searched for outer halo star clusters in M33 as part of the Pan-Andromeda Archaeological Survey using the images taken with the Canada–France–Hawaii Telescope/MegaCam, and found one new unambiguous star cluster in addition to the five previously known in the M33 outer halo, and determined structural parameters for these six outer halo clusters.

From Figure 4, we can see that for the data of Galactic GCs which were updated in 2010, in addition to the clusters already noted by Mackey & van den Bergh (2005), i.e., M54 (NGC 6715), ω Cen (NGC 5139), NGC 2419, there are three other bright GCs (NGC 104, NGC 5272, and NGC 5024) lying above the "ordinary globular clusters" threshold. For M31 star clusters, in addition to G1, there are 26 other bright clusters lying above the line defined by Equation (3). All of these objects are classified as GCs (Barmby et al. 2007; Mackey et al. 2007) or bright young clusters (Barmby et al. 2009). For four extended luminous GCs in the outskirts of M31, they all lie above the line defined by Equation (3).

Based on F606W and F814W images of B514 obtained with the ACS/*HST* (program ID GO 10565; PI: S. Galleti), Federici et al. (2007) also studied in detail its surface brightness distribution in the F606W and F814W filters and determined its structural parameters by fitting a King (1962) model to a surface brightness profile. Comparing the results of Federici et al. (2007) with Table 6 of this paper, we find that our model fits produce smaller tidal radii, which result in smaller half-light, or effective, radii of a model. In addition, Federici et al. (2007) adopted $M_V = -9.1$ being brighter than $M_V = -9.02$ adopted here. So, in Federici et al. (2007), B514 lies above and brightward of the line defined by Equation (3).

3. ARCHIVAL IMAGES OF THE BATC MULTICOLOR SKY SURVEY, 2MASS, AND *GALEX* AND PHOTOMETRIC DATA OF SDSS

In this section, we will determine the magnitudes of B514 based on the archival images of the BATC Multicolor Sky

Table 6
Structural Parameters of B514

Parameters	F606W	F814W
r_0	$0.36^{+0.09}_{-0.05}$ arcsec($= 1.35^{+0.35}_{-0.19}$ pc)	$0.36^{+0.09}_{-0.06}$ arcsec($= 1.35^{+0.32}_{-0.22}$ pc)
r_t	$16.08^{+2.11}_{-1.35}$ arcsec($= 61.11^{+8.00}_{-5.14}$ pc)	$16.79^{+1.74}_{-1.48}$ arcsec($= 63.78^{+6.62}_{-5.64}$ pc)
$c = \log(r_t/r_0)$	$1.66^{+0.05}_{-0.04}$	$1.68^{+0.04}_{-0.04}$
r_h	$1.31^{+0.14}_{-0.08}$ arcsec($= 5.00^{+0.55}_{-0.32}$ pc)	$1.36^{+0.13}_{-0.09}$ arcsec($= 5.17^{+0.48}_{-0.34}$ pc)
μ_0 (mag arcsec^{-2})	$16.25^{+0.57}_{-0.56}$	$15.64^{+0.80}_{-0.64}$

Table 7
BATC Photometry of B514

Filter	Central Wavelength (Å)	Bandwidth (Å)	Number of Images	Exposure Time (hr)	rms (mag)	Magnitude
a	3360	222	6	2:00	0.010	17.59 ± 0.05
b	3890	187	6	2:00	0.010	16.82 ± 0.02
c	4210	185	4	1:00	0.002	16.52 ± 0.01
d	4550	222	4	1:20	0.015	16.25 ± 0.02
e	4920	225	3	1:00	0.007	16.05 ± 0.01
f	5270	211	3	1:00	0.014	15.85 ± 0.02
g	5795	176	3	1:00	0.010	15.64 ± 0.01
h	6075	190	3	0:50	0.005	15.56 ± 0.01
i	6660	312	3	0:50	0.004	15.44 ± 0.01
j	7050	121	3	1:00	0.006	15.33 ± 0.01
k	7490	125	3	1:00	0.011	15.25 ± 0.01
m	8020	179	3	1:00	0.003	15.19 ± 0.01
n	8480	152	3	1:00	0.005	15.12 ± 0.01

Survey, 2MASS, and *Galaxy Evolution Explorer* (*GALEX*) using a standard aperture photometry approach, i.e., the PHOT routine in DAOPHOT (Stetson 1987). In addition, we will introduce the photometric data of B514 from the Sloan Digital Sky Survey (SDSS) obtained by Peacock et al. (2010).

3.1. Intermediate-band Photometry of B514

Observations of B514 were also obtained with the BATC 60/90 cm Schmidt telescope located at the Xinglong station of the National Astronomical Observatory of China (NAOC). This telescope is equipped with 15 intermediate-band filters covering the optical wavelength range from 3000 to 10000 Å (see Fan et al. 2009 for details). Figure 5 shows a finding chart of B514 in the BATC *b* band (centered at 5795 Å).

The BATC survey team obtained 47 images of B514 in 13 BATC filters between 2005 March 1 and 2006 December 9. Table 7 contains the observation log, including the BATC filter names, the central wavelength and bandwidth of each filter, the number of images observed through each filter, and the total observing time per filter. Multiple images through the same filter were combined to improve image quality (i.e., increase the S/N and remove spurious signal).

Calibration of the magnitude zero level in the BATC photometric system is similar to that of the spectrophotometric AB magnitude system. For flux calibration, the Oke–Gunn (Oke & Gunn 1983) primary flux standard stars HD 19445, HD 84937, BD +26°2606, and BD +17°4708 were observed during photometric nights (Yan et al. 2000). Column 6 of Table 7 gives the zero-point errors in magnitude for the standard stars through each filter. The formal errors obtained for these stars in the 13 BATC filters used are $\lesssim$0.02 mag, which implies that we can define photometrically the BATC system to an accuracy of better than 0.02 mag.

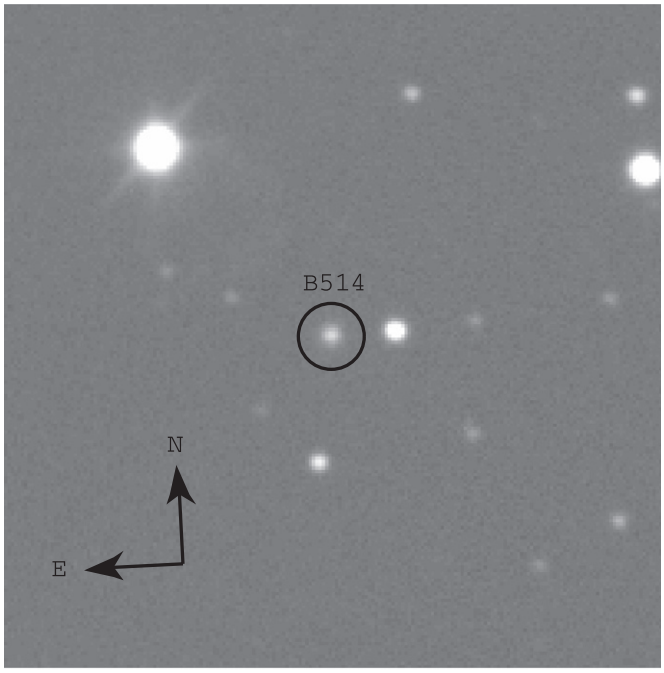

Figure 5. Image of B514 in the BATC *b* band, obtained with the NAOC 60/90 cm Schmidt telescope. B514 is circled using an aperture with a radius of 13″. The field of view of the image is 4.′3 × 4.′3.

We determined the intermediate-band magnitudes of B514 on the combined images. The (radial) photometric asymptotic growth curves in all BATC bands flatten out at a radius of ∼13″. Inspection ensured that this aperture is adequate for photometry, i.e., B514 does not show any obvious signal beyond this radius. Therefore, we use an aperture with $r \approx 13''$ for integrated photometry. Since B514 is located in the

Table 8
2MASS and *GALEX* Photometry of B514

Filter	Magnitude
J	14.23 ± 0.07
H	13.32 ± 0.06
K_s	13.63 ± 0.10
NUV	19.57 ± 0.86
FUV	20.44 ± 2.30

M31 halo, contamination from background fluctuations can be neglected. We adopted annuli for background subtraction spanning between 14″ and 20″. The calibrated photometry of B514 in 13 filters is summarized in Column 7 of Table 7, in conjunction with the 1σ magnitude uncertainties, which include uncertainties from the calibration errors in magnitude from DAOPHOT.

3.2. Near-infrared 2MASS Photometry of B514

B514 was detected by Galleti et al. (2005) based on the XSC sources of the All Sky Data Release of 2MASS within a $\sim 9^\circ \times 9^\circ$ area centered on M31. In order to obtain accurate photometry for B514 in JHK_s, we download the images in JHK_s filters including B514. The image in each filter is combined using six frames of 1.3 s, so the total exposure time of the image in each filter is 7.8 s. The mosaic pixel scale of the final atlas image is resampled to 1″ (see Skrutskie et al. 2006 for details). The relevant zero points for photometry are 20.9210, 20.7089, and 20.0783 in J, H, and K_s magnitudes, respectively, which are presented in photometric header keywords. We use an aperture with $r = 13''$ for integrated photometry, and annuli for background subtraction spanning between 14″ and 19″. The calibrated photometry of B514 in the J, H, and K_s filters is summarized in Table 8, in conjunction with the 1σ magnitude uncertainties obtained from DAOPHOT.

3.3. GALEX Ultraviolet Photometry of B514

While the principal science goal of the *GALEX* (Martin et al. 2005; Morrissey et al. 2007) has been the study of star formation in the local and intermediate-redshift universe, nearby galaxies such as M31 have also been surveyed, taking advantage of the wide (1.°2) field of view of *GALEX*. The B514 images were obtained as part of the guest program carried out by *GALEX* in two UV bands: far-ultraviolet (FUV; $\lambda_{\rm eff} = 1539$ Å, FWHM ≈ 270 Å) and near-ultraviolet (NUV; $\lambda_{\rm eff} = 2316$ Å, FWHM ≈ 615 Å) with resolutions of 4.″2 (FUV) and 5.″3, respectively (NUV; Morrissey et al. 2007). The exposure times are 1616 s in FUV and 1704 s in NUV. The images are sampled with 1.″5 pixels. The data were downloaded from the MAST archive. The relevant zero points for photometry are 20.08 and 18.82 in NUV and FUV magnitudes, respectively (Morrissey et al. 2007). We use an aperture with $r = 12''$ for integrated photometry, and annuli for background subtraction spanning between 13.″5 and 19.″5. The calibrated photometry of B514 in the NUV and FUV filters is summarized in Table 8. From Table 8, we can see that the 1σ magnitude uncertainties are great, especially if the magnitude uncertainty in FUV is very great (2.3 mag), i.e., the S/Ns of these images are low, especially if the S/N of the image in FUV is very low. Since the magnitude uncertainty in FUV is very great, we will not use it when fitting to derive the age of B514 in Section 4.

3.4. Photometric Data of B514 from SDSS

Peacock et al. (2010) presented an updated catalog of M31 GCs based on images from the Wide Field Camera (WFCAM) on the United Kingdom Infrared Telescope and from the SDSS, in which $ugriz$ and K-band photometry are determined. In this catalog, B514 is named H6 from Huxor et al. (2008) and $ugriz$ photometry is presented.

4. STELLAR POPULATION OF B514

4.1. Metallicity of B514

Cluster SEDs are determined by the combination of their ages and metallicities, which is often referred to as the age–metallicity degeneracy. Therefore, the age of a cluster can only be constrained accurately if the metallicity is known with confidence, from independent determinations. There exist four metallicity determinations for B514, namely, [Fe/H] $= -1.8 \pm 0.3$ (spectroscopic from Galleti et al. 2005), -1.8 ± 0.15 (from the CMD; Galleti et al. 2006), -2.14 ± 0.15 (from the CMD; Mackey et al. 2007), and -2.06 ± 0.16 (spectroscopic from Galleti et al. 2009), which are consistent. In order to adopt a reasonable value of metallicity for B514, the mean value of these four independent determinations, i.e., [Fe/H] $= -1.95$, is adopted in this paper.

4.2. Stellar Populations and Synthetic Photometry

To determine the age and mass of B514, we compared its SEDs with theoretical stellar population synthesis models. The SEDs consist of photometric data from the NUV of *GALEX*, 13 BATC intermediate-band filters, and 2MASS near-infrared JHK_s filters obtained in this paper, and of the photometric data in five SDSS filters obtained by Peacock et al. (2010). We will not include the photometric datum in the FUV band when constraining the age of B514 because of its large photometric error (2.3 mag), i.e., the photometric datum is not accurate. B514 is a very metal-poor GC (see discussions above). Hence, we use the SSP models of Bruzual & Charlot (2003, hereafter BC03), which have been upgraded from the earlier Bruzual & Charlot (1993) and A. G. Bruzual & S. Charlot (1996, unpublished) versions, and now provide the evolution of the spectra and photometric properties for a wide range of stellar metallicities. For example, BC03 SSP models based on the Padova 1994 evolutionary tracks include six initial metallicities, $Z = 0.0001, 0.0004, 0.004, 0.008, 0.02\,(Z_\odot)$, and 0.05, corresponding to [Fe/H] $= -2.25, -1.65, -0.64, -0.33,$ +0.09, and +0.56. BC03 provides 26 SSP models (both of high and low spectral resolution) using the Padova 1994 evolutionary tracks, half of which were computed based on the Salpeter (1955) initial mass function (IMF) with lower and upper mass cutoffs of $m_{\rm L} = 0.1\,M_\odot$ and $m_{\rm U} = 100\,M_\odot$, respectively. The other 13 were computed using the Chabrier (2003) IMF with the same mass cutoffs. In addition, BC03 provide 26 SSP models using the Padova 2000 evolutionary tracks which include 6 partially different initial metallicities, $Z = 0.0004, 0.001, 0.004, 0.008, 0.019\,(Z_\odot)$, and 0.03, i.e., [Fe/H] $= -1.65, -1.25, -0.64, -0.33, +0.07$, and +0.29. In this paper, we adopt the high-resolution SSP models using the Padova 1994 evolutionary tracks to determine the most appropriate age for B514 since its metallicity is [Fe/H] $= -1.95$, and a Salpeter (1955) IMF is used. These SSP models contain 221 spectra describing the spectral evolution of SSPs from 1.0×10^5 yr to 20 Gyr. The evolving spectra include the

Table 9
Mass Estimates (and Uncertainties) of B514 Based on the BC03 Models

V	u	g	r	i	z	J	H	K_s
Mass ($10^6\ M_\odot$)								
1.08 ± 0.03	0.99 ± 0.03	1.06 ± 0.03	1.02 ± 0.03	1.0 ± 0.03	0.98 ± 0.03	0.98 ± 0.06	1.41 ± 0.08	0.96 ± 0.09

contribution of the stellar component at wavelengths from 91 Å to 160 μm.

Since our observational data are integrated luminosities through a given set of filters, we convolved the theoretical SSP SEDs of BC03 with the *GALEX* NUV, SDSS $ugriz$, BATC $a-n$, and 2MASS JHK_s filter response curves to obtain synthetic optical and NIR photometry for comparison (see Ma et al. 2009a, 2009b, 2011; Wang et al. 2010 for details).

4.3. Fit Results

We use a χ^2 minimization approach to examine which SSP models are most compatible with the observed SEDs, following

$$\chi^2 = \sum_{i=1}^{22} \frac{\left[m_{\lambda_i}^{\rm intr} - m_{\lambda_i}^{\rm mod}(t)\right]^2}{\sigma_i^2}, \quad (4)$$

where $m_{\lambda_i}^{\rm mod}(t)$ is the integrated magnitude in the ith filter of a theoretical SSP at age t, $m_{\lambda_i}^{\rm intr}$ represents the intrinsic integrated magnitude in the same filter, and σ_i is the magnitude uncertainty, defined as

$$\sigma_i^2 = \sigma_{{\rm obs},i}^2 + \sigma_{{\rm mod},i}^2 + \sigma_{{\rm md},i}^2. \quad (5)$$

Here, $\sigma_{{\rm obs},i}$ is the observational uncertainty from Tables 7 and 8 of this paper, and Table 1 of Peacock et al. (2010), $\sigma_{{\rm mod},i}$ is the uncertainty associated with the model itself, and $\sigma_{{\rm md},i}$ is associated with the uncertainty with the distance modulus adopted here. Charlot et al. (1996) estimated the uncertainty associated with the term $\sigma_{{\rm mod},i}$ by comparing the colors obtained from different stellar evolutionary tracks and spectral libraries. Following Ma et al. (2009a), Ma et al. (2009b), Wang et al. (2010), and Ma et al. (2011), we adopt $\sigma_{{\rm mod},i} = 0.05$ mag. For $\sigma_{{\rm md},i}$, we adopt 0.07 from McConnachie et al. (2005).

Before fitting, we obtained the theoretical SEDs for the metallicity [Fe/H] $= -1.95$ model by interpolation between [Fe/H] $= -2.25$ and -1.65 models.

Since the observed magnitudes in the 2MASS photometric systems are given in the Vega system, we transformed them to the AB system for our fits. The photometric offsets in the 2MASS filters between the Vega and AB systems were obtained based on Equations (7) and (8) in the manual provided by Bruzual & Charlot (2003; bc03.ps). The best-reduced $\chi^2_{\rm min}/\nu = 0.8$ is achieved with an age of 11.5 ± 3.5 Gyr (1σ uncertainties), $\nu = 21$ is the number of free parameters, i.e., the number of observational data points minus the number of parameters used in the theoretical model. In Figure 6, we show the intrinsic SEDs of B514 and the integrated SEDs and spectra of the best-fitting model. From Figure 6, we can see that the BC03 SSP models cannot fit the photometric data point in the H band as well as the other 21 data points, i.e., the observed magnitude is brighter than the model one in the H band. However, the photometric data point in the H band from Galleti et al. (2005) can be fitted by BC03 SSP models as well as the other 21 data points, and the fitting result (the age of B514) is in agreement with the one obtained above (11.5 ± 3.5 Gyr) within the uncertainty.

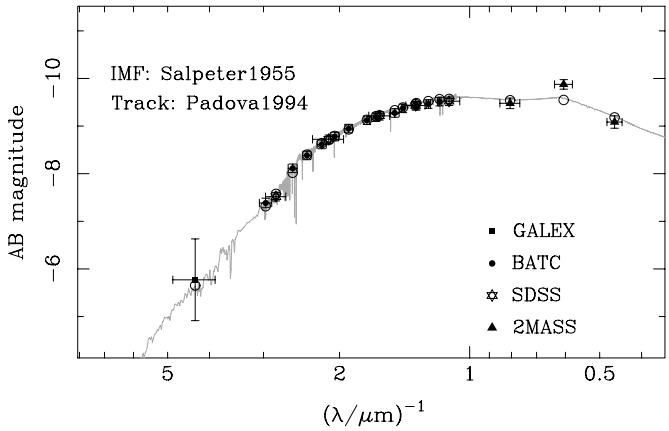

Figure 6. Best-fitting, integrated theoretical BC03 SEDs compared to the intrinsic SED of B514. The photometric measurements are shown as symbols with error bars. The open circles represent the calculated magnitudes of the model SED for each filter.

4.4. Mass of B514

Next we determined the mass of B514. The BC03 SSP models are normalized to a total mass of 1 $M_\odot$ in stars at age $t = 0$. The absolute magnitudes (in the Vega system) in V, SDSS $ugriz$, and 2MASS JHK_s filters are included in the BC03 SSP models. The difference between the intrinsic absolute magnitudes and those given by the model provides a direct measurement of the cluster mass. To reduce mass uncertainties resulting from photometric uncertainties based on only magnitudes in one filter (in general, the V band is used), we estimated the mass of B514 using magnitudes in the V, $ugriz$, and JHK_s bands. The resulting mass determinations for B514 are listed in Table 9 with their 1σ uncertainties. From Table 9, we can see that the mass of B514 obtained based on the magnitudes in different filters is consistent except for one in the H band. In fact, the observed magnitude is brighter than the model magnitude in the H band (see discussion in Section 4.3). So, the mass of B514 derived based on the magnitude in the H band is more massive than its true mass. The mass of B514 derived based on the magnitude in the H band from Galleti et al. (2005) is in agreement with ones derived based on the magnitudes in the other eight bands (Table 9). We know that the obtained mass of B514 is between 0.96 and $1.08 \times 10^6\ M_\odot$ not including the one in the H band. Compared with 037-B327 ($\mathcal{M}_{\rm 037\text{-}B327} \sim 8.5 \times 10^6\ M_\odot$, Barmby et al. 2002, or $\mathcal{M}_{\rm 037\text{-}B327} \sim 3.0 \pm 0.5 \times 10^7\ M_\odot$, Ma et al. 2006a) and G1 ($\mathcal{M}_{\rm G1} \sim$ (7–17) $\times 10^6\ M_\odot$, Meylan et al. 2001, or $\mathcal{M}_{\rm G1} \sim$ (5.8–10.6) $\times 10^6\ M_\odot$, Ma et al. 2009a) in M31 and ω Cen ($\mathcal{M}_{\omega{\rm Cen}} \sim$ (2.9–5.1) $\times 10^6\ M_\odot$; Meylan 2002) in the Milky Way, the most massive clusters in the Local Group, B514 is only a medium-mass GC.

5. SUMMARY

In this paper, we determined the structural parameters of the remote GC B514 known in M31 based on F606W and F814W images obtained with the ACS/*HST*. By performing a fit to

the surface brightness distribution of a single-mass isotropic King model, we derive its parameters: the best-fitting scale radii $r_0 = 0.36^{+0.09}_{-0.05}$ arcsec(= $1.35^{+0.35}_{-0.19}$ pc) and $0.36^{+0.09}_{-0.06}$ arcsec(= $1.35^{+0.32}_{-0.22}$ pc), tidal radii $r_t = 16.08^{+2.11}_{-1.35}$ arcsec(= $61.11^{+8.00}_{-5.14}$ pc) and $16.79^{+1.74}_{-1.48}$ arcsec(= $63.78^{+6.62}_{-5.64}$ pc), and concentration indexes $c = \log(r_t/r_0) = 1.66^{+0.05}_{-0.04}$ and $1.68^{+0.04}_{-0.04}$ in F606W and F814W, respectively; the central surface brightnesses are $16.25^{+0.57}_{-0.56}$ mag arcsec^{-2} and $15.64^{+0.80}_{-0.64}$ mag arcsec^{-2} in F606W and F814W, respectively; and the half-light, or effective, radius of a model that contains half the total luminosity in projection, at $r_h = 1.31^{+0.14}_{-0.08}$ arcsec(= $5.00^{+0.55}_{-0.32}$ pc) and $1.36^{+0.13}_{-0.09}$ arcsec(= $5.17^{+0.48}_{-0.34}$ pc) in F606W and F814W, respectively. The results show that the surface brightness distribution departs from the best-fit King model for $r > 10''$. In addition, B514 was observed as part of the BATC Multicolor Sky Survey, using 13 intermediate-band filters covering a wavelength range of 3000–80000 Å. Based on aperture photometry, we obtain its SEDs as defined by the 13 BATC filters. We determine the cluster's age by comparing its SEDs (from 2267 to 20000 Å, comprised of photometric data in the NUV of *GALEX*, 13 BATC intermediate-band filters, and five SDSS filters, and 2MASS near-infrared JHK_s data) with theoretical stellar population synthesis models, resulting in an age of 11.5 ± 3.5 Gyr. This age confirms previous suggestions that B514 is an old GC in M31. B514 has a mass of $0.96–1.08 \times 10^6\ M_\odot$ and is a medium-mass GC in M31.

We thank the anonymous referee for providing a rapid and thoughtful report that helped improve the original manuscript greatly. This work is partly based on observations made with the NASA/ESA *Hubble Space Telescope*, obtained at the Space Telescope Science Institute, which is operated by AURA, Inc., under NASA contract NAS 5-26555. These observations are associated with proposal 10394. This work was supported by the Chinese National Natural Science Foundation grant Nos. 10873016, 10633020, 10803007, 11003021, and 11073032, and by the National Basic Research Program of China (973 Program) No. 2007CB815403.

REFERENCES

Barmby, P., Holland, S., & Huchra, J. 2002, AJ, 123, 1937
Barmby, P., & Huchra, J. P. 2001, AJ, 122, 2458
Barmby, P., Huchra, J., Brodie, J., et al. 2000, AJ, 119, 727
Barmby, P., McLaughlin, D. E., Harris, W. E., Harris, G. L. H., & Forbes, D. A. 2007, AJ, 133, 2764
Barmby, P., Perina, S., Bellazzini, M., et al. 2009, AJ, 138, 1667
Battistini, P., Bònoli, F., Braccesi, A., et al. 1980, A&AS, 42, 357
Battistini, P., Bònoli, F., Braccesi, A., et al. 1987, A&AS, 67, 447
Battistini, P., Bònoli, F., Casavecchia, M., et al. 1993, A&A, 272, 77
Beasley, M. A., Brodie, J. P., Strader, J., et al. 2004, AJ, 128, 1623
Bik, A., Lamers, H. J. G. L. M., Bastian, N., Panagia, N., & Romaniello, M. 2003, A&A, 397, 473
Brodie, J. P., & Strader, J. 2006, ARA&A, 44, 193
Brown, T. M., Ferguson, H. C., Smith, E., et al. 2004, ApJ, 613, L125
Bruzual, A. G., & Charlot, S. 1993, ApJ, 405, 538
Bruzual, A. G., & Charlot, S. 2003, MNRAS, 344, 1000
Caldwell, N., Harding, P., Morrison, H., et al. 2009, AJ, 137, 94
Caldwell, N., Schiavon, R., Morrison, H., Rose, J. A., & Harding, P. 2011, AJ, 141, 61
Cardelli, J. A., Clayton, G. C., & Mathis, J. S. 1989, ApJ, 345, 245
Chabrier, G. 2003, PASP, 115, 763
Charlot, S., Worthey, G., & Bressan, A. 1996, ApJ, 457, 625
Clementini, G., Contreras, R., Federici, L., et al. 2009, ApJ, 704, L103
Cockcroft, R., Harris, W. E., Ferguson, A. M. N., et al. 2011, ApJ, 730, 112
de Grijs, R., Anders, P., Lynds, R., et al. 2003a, MNRAS, 343, 1285
de Grijs, R., Bastian, N., & Lamers, H. J. G. L. M. 2003b, MNRAS, 340, 197
de Grijs, R., Fritze-v. Alvensleben, U., Anders, P., et al. 2003c, MNRAS, 342, 259
de Grijs, R., Wilkinson, M. I., & Tadhunter, C. N. 2005, MNRAS, 361, 311
Dolphin, A. E. 2000a, PASP, 112, 1383
Dolphin, A. E. 2000b, PASP, 112, 1397
Elson, R. A. W., Fall, S. M., & Freeman, K. C. 1987, ApJ, 323, 54
Fan, Z., Ma, J., de Grijs, R., Yang, Y., & Zhou, X. 2006, MNRAS, 371, 1648
Fan, Z., Ma, J., & Zhou, X. 2009, Res. Astron. Astrophys., 9, 993
Federici, L., Bellazzini, M., Galleti, S., et al. 2007, A&A, 473, 429
Freeman, K. C. 1993, in IAU Symp. 153, Galactic Bulges, ed. H. Dejonghe & H. J. Habing (Dordrecht: Kluwer), 263
Frogel, J. A., Persson, S. E., & Cohen, J. G. 1980, ApJ, 240, 785
Fusi Pecci, F., Bellazini, M., De Simone, E., & Federici, L. 2005, AJ, 130, 544
Fusi Pecci, F., Cacciari, C., Federici, L., & Pasquali, A. 1993, in ASP Conf. Ser. 48, The Globular Cluster–Galaxy Connection, ed. G. H. Smith & J. P. Brodie (San Francisco, CA: ASP), 410
Galleti, S., Bellazzini, M., Buzzoni, A., Federici, L., & Fusi Pecci, F. 2009, A&A, 508, 1285
Galleti, S., Bellazzini, M., Federici, L., Buzzoni, A., & Fusi Pecci, F. 2007, A&A, 471, 127
Galleti, S., Bellazzini, M., Federici, L., & Fusi Pecci, F. 2005, A&A, 436, 535
Galleti, S., Federici, L., Bellazzini, M., Buzzoni, A., & Fusi Pecci, F. 2006, ApJ, 650, L107
Galleti, S., Federici, L., Bellazzini, M., Fusi Pecci, F., & Macrina, S. 2004, A&A, 426, 917
Harris, W. E. 1991, ARA&A, 29, 543
Harris, W. E. 1996, AJ, 112, 1487
Harris, W. E., Harris, G. L. H., Holland, S. T., & McLaughlin, D. E. 2002, AJ, 124, 1435
Henon, M. 1973, A&A, 24, 229
Hodge, P. W. 1992, The Andromeda Galaxy (Dordrecht: Kluwer)
Holland, S. 1998, AJ, 115, 1916
Hubble, E. P. 1932, ApJ, 76, 44
Huxor, A. P., Ferguson, A. M. N., Tanvir, N. R., et al. 2011, MNRAS, 414, 770
Huxor, A. P., Tanvir, N. R., Ferguson, A. M. N., et al. 2008, MNRAS, 385, 1989
Huxor, A. P., Tanvir, N. R., Irwin, M. J., et al. 2005, MNRAS, 360, 1007
Jiang, L., Ma, J., Zhou, X., et al. 2003, AJ, 125, 727
Kim, S. C., Lee, M. G., Geisler, D., et al. 2007, AJ, 134, 706
King, I. 1962, AJ, 67, 471
King, I. 1966, AJ, 71, 64
Larsen, S. S., Brodie, J. P., Sarajedini, A., & Huchra, J. P. 2002, AJ, 124, 2615
Lightman, A. P., & Shapiro, S. L. 1978, Rev. Mod. Phys., 50, 437
Ma, J. 2011, Res. Astron. Astrophys., 11, 524
Ma, J., de Grijs, R., Chen, D., et al. 2007a, MNRAS, 376, 1621
Ma, J., de Grijs, R., Fan, Z., et al. 2009a, Res. Astron. Astrophys., 9, 641
Ma, J., de Grijs, R., Yang, Y., et al. 2006a, MNRAS, 368, 1443
Ma, J., Fan, Z., de Grijs, R., et al. 2009b, AJ, 137, 4884
Ma, J., van den Bergh, S., Wu, H., et al. 2006b, ApJ, 636, L93
Ma, J., Wang, S., Wu, Z., et al. 2011, AJ, 141, 86
Ma, J., Yang, Y., Burstein, D., et al. 2007b, ApJ, 659, 359
Mackey, A. D., Ferguson, A. M. N., Irwin, M. J., et al. 2010, MNRAS, 401, 533
Mackey, A. D., Huxor, A., Ferguson, A. M. N., et al. 2006, ApJ, 653, L105
Mackey, A. D., Huxor, A., Ferguson, A. M. N., et al. 2007, ApJ, 655, L85
Mackey, A. D., & van den Bergh, S. 2005, MNRAS, 360, 631
Martin, D. C., Fanson, J., Schiminovich, D., et al. 2005, ApJ, 619, L1
Martin, N. F., Ibata, R. A., Irwin, M. J., et al. 2006, MNRAS, 371, 1983
McClure, R. D., & Racine, R. 1969, AJ, 74, 1000
McConnachie, A. W., Irwin, M. J., Ferguson, A. M. N., et al. 2005, MNRAS, 356, 979
McLaughlin, D. E., Barmby, P., Harris, W. E., Forbes, D. A., & Harris, G. L. H. 2008, MNRAS, 384, 563
McLaughlin, D. E., & van der Marel, R. P. 2005, ApJS, 161, 304
Meylan, G. 2002, in IAU Symp. 207, Extragalactic Star Clusters, ed. D. Geisler, E. K. Grevel, & D. Minniti (San Francisco, CA: ASP), 555
Meylan, G., Sarajedini, A., Jablonka, P., et al. 2001, AJ, 122, 830
Michie, R. W. 1963, MNRAS, 125, 127
Mochejska, B. J., Kaluzny, J., Krockenberger, M., Sasselov, D. D., & Stanek, K. Z. 1998, Acta Astron., 48, 455
Morrissey, P., Conrow, T., Barlow, T. A., et al. 2007, ApJS, 173, 682
Murphy, B. W., Cohn, H. N., & Hut, P. 1990, MNRAS, 245, 335
Oke, J. B., & Gunn, J. E. 1983, ApJ, 266, 713
Peacock, M. B., Maccarone, T. J., Knigge, C., et al. 2010, MNRAS, 402, 803
Perina, S., Barmby, P., Beasley, M. A., et al. 2009, A&A, 494, 933
Perina, S., Galleti, S., Fusi Pecci, F., et al. 2011, A&A, 531, 155
Puzia, T. H., Perrett, K. M., & Bridges, T. J. 2005, A&A, 434, 909
Puzia, T. H., Zepf, S. E., Kissler-Patig, M., et al. 2002, A&A, 391, 453
Racine, R. 1991, AJ, 101, 865

Rich, R. M., Shara, M. M., & Zurek, D. 2001, AJ, 122, 842
Salpeter, E. E. 1955, ApJ, 121, 161
Sérsic, J.-L. 1968, Atlas de Galaxias Australes (Cordoba: Observatoria Astronomico)
Sirianni, M., Jee, M. J., Benítez, N., et al. 2005, PASP, 117, 1049
Skrutskie, M. F., Cutri, R. M., Stiening, R., et al. 2006, AJ, 131, 1163
Spitzer, L., & Thuan, T. X. 1972, ApJ, 175, 31
Stanek, K. Z., & Garnavich, P. M. 1998, ApJ, 503, 131
Stetson, P. B. 1987, PASP, 99, 191
Trager, S. C., King, I. R., & Djorgovski, S. 1995, AJ, 109, 218
van den Bergh, S. 1969, ApJS, 19, 145
van den Bergh, S., & Mackey, A. D. 2004, MNRAS, 354, 713
Wang, S., Fan, Z., Ma, J., de Grijs, R., & Zhou, X. 2010, AJ, 139, 1438
Williams, B. F., & Hodge, P. W. 2001a, ApJ, 548, 190
Williams, B. F., & Hodge, P. W. 2001b, ApJ, 559, 851
Wilson, C. P. 1975, AJ, 80, 175
Yan, H., Burstein, D., Fan, X., et al. 2000, PASP, 112, 691
Zinnecker, H., Keable, C. J., Dunlop, J. S., Cannon, R. D., & Griffiths, W. K. 1988, in IAU Symp. 126, The Harlow–Shapley Symposium on Globular Cluster Systems in Galaxies, ed. J. E. Grindlay & A. G. D. Philip (Dordrecht: Kluwer), 603